Article

Back Contact Engineering to Improve CZTSSe Solar Cell Performance by Inserting MoO$_3$ Sacrificial Nanolayers

Cheng-Ying Chen [1,2,*,†] , Septia Kholimatussadiah [2,3,4,5,†], Wei-Chao Chen [2,6], Yi-Rung Lin [2,3,6], Jia-Wei Lin [2,3,7], Po-Tuan Chen [2,3,8], Ruei-San Chen [9], Kuei-Hsien Chen [2,6] and Li-Chyong Chen [2,3,4]

1   Department of Optoelectronics and Materials Technology, National Taiwan Ocean University, Keelung City 202301, Taiwan
2   Center for Condensed Matter Sciences, National Taiwan University, Taipei 10617, Taiwan; d08222017@ntu.edu.tw (S.K.); weichao.chen@solidedgesolution.com (W.-C.C.); d98223132@ntu.edu.tw (Y.-R.L.); r07527025@ntu.edu.tw (J.-W.L.); potuan@ntut.edu.tw (P.-T.C.); chenkh@pub.iams.sinica.edu.tw (K.-H.C.); chenlc@ntu.edu.tw (L.-C.C.)
3   Center of Atomic Initiative for New Materials, National Taiwan University, Taipei 10617, Taiwan
4   Department of Physics, National Taiwan University, Taipei 10617, Taiwan
5   Nano Science and Technology Program, Taiwan International Graduate Program, Academia Sinica, Taipei 115, Taiwan
6   Institute of Atomic and Molecular Sciences, Academia Sinica, Taipei 10617, Taiwan
7   Department of Materials Science and Engineering, National Taiwan University, Taipei 10617, Taiwan
8   Department of Vehicle Engineering, National Taipei University of Technology, Taipei 10608, Taiwan
9   Graduate Institute of Applied Science and Technology, National Taiwan University of Science and Technology, Taipei 10617, Taiwan; rsc@mail.ntust.edu.tw
*   Correspondence: cychen0111@mail.ntou.edu.tw
†   These authors contributed equally to this work.

Abstract: Earth-abundant Cu$_2$ZnSn(S,Se)$_4$ (CZTSSe) is a promising nontoxic alternative compound for commercially available Cu(In,Ga)(S,Se)$_2$ thin-film solar cells. In this study, a MoO$_3$ nanolayer was applied as a sacrificial layer to optimize the quality of the interface between the CZTSSe and Mo back contact. MoO$_3$ nanolayers can greatly improve CZTSSe grain growth and suppress the formation of some harmful secondary phases, especially the undesirable MoS(e)$_2$. In terms of device performance, the series resistance was reduced from 1.83 to 1.54 $\Omega \cdot$cm^2, and the fill factor was significantly enhanced from 42.67% to 52.12%. Additionally, MoO$_3$ nanolayers improved CZTSSe absorber quality by lowering the defect energy levels from 228 to 148 meV. Furthermore, first-principles calculations demonstrate that the partial sulfoselenized MoO$_3$ nanolayers may function as the (*p*-type) hole-selective contacts at Mo/CZTSSe interfaces, leading to an overall improvement in device performance. Lastly, a CZTSSe solar cell with about 26% improvement (compared with reference cells) in power conversion efficiency was achieved by inserting 5 nm MoO$_3$ sacrificial layers.

Keywords: CZTSSe; Earth-abundant materials; back contacts; MoO$_3$; solar cells; hole-selective contacts

1. Introduction

Thin-film chalcogenide-based solar cells such as CdTe [1] and Cu(In,Ga)(S,Se)$_2$ (CIGSSe) [2–4] are commercially available and demonstrate over 20% power conversion efficiency (PCE). However, the toxicity of cadmium (Cd), and the scarcity of indium (In) and tellurium (Te) are major concerns for their applications [5,6]. Meanwhile, Earth-abundant and nontoxic CZTSSe, which shows a tunable direct bandgap of 1.1–1.5 eV by varying the S/Se ratio and high absorption coefficient of over 10^4 cm^{-1} [7–9], is treated as a promising alternative for CdTe and CIGSSe [10,11]. However, the open-circuit voltage (V$_{OC}$) deficit and low fill factor (FF) critically obstruct PCE in CZTSSe solar cells, with the highest efficiency reaching 12.6% [12], which is significantly lower than the established chalcogenide absorbers [4]. On the basis of the existing configuration of CIGSSe solar cells, molybdenum

(Mo) is also used as the back contact for CZTSSe. Nevertheless, Mo induces the detrimental decomposition of CZTSSe and the formation of performance-harmful binary secondary phases, such as $Cu_xS(e)_y$, $Sn_xS(e)_y$ and $Zn_xS(e)_y$, leading to some voids near the back sides, and $MoS(e)_2$ [13]. Although $MoS(e)_2$ improves the adhesion and quasiohmic contact if it is thin enough [14–16], thick $MoS(e)_2$ is more likely to be formed due to a required high sulfur (S) and/or selenium (Se) pressure [17] during the formation of a CZTSSe absorber. Moreover, CZTS-based absorbers are generally chalcogen-poor, and S/Se vacancies are classified as deep-level defects [18] leading to high series resistance (Rs), thus degrading the overall solar cell performance, especially the V_{OC} deficit and low FF [17].

In order to suppress thick $MoS(e)_2$ formation, several different intermediate layers were introduced between the CZTSSe absorber and Mo back contact, such as TiN [17,19], TiB_2 [20], carbon [21], and ZnO [22]. In this regard, introducing a very thin MoO_x at the interface between CZTSSe and Mo back contact can be advantageous because it may modify the surface energy of the Mo substrate and thus further enhance CZTSSe grain growth. From a band alignment point of view, oxidized MoS_2 (i.e., $MoS_{2-x}O_x$) layers with *p*-type conductivity are also preferred [23–27]. N-type MoS_2 layers with low work function are not suitable for the hole-transporting contact with *p*-type CZTSSe because it may form another *p*–n junction. In solar cell devices with nonohmic contacts, the V_{OC} is limited by the work function difference between the top and bottom electrodes instead of the quasi-Fermi level splitting of the absorbers [10,28]. Therefore, MoO_x can be a promising sacrificial material because not only the formation of a conductive *p*-type $MoS(e)_{2-x}O_x$ layer is beneficial, but also the voids and unwanted secondary phases can be inhibited by avoiding direct reaction between CZTSSe and Mo.

In this work, we utilized a thermally evaporated ultrathin MoO_3 nanolayer as a sacrificial layer to optimize the back contact interface between CZTSSe and Mo. Cross-sectional transmission electron macroscopy (TEM) combined with energy-dispersive X-ray spectroscopy (EDS) results confirmed that the sacrificial nanolayers increase grain growth (from ~800 to ~1000 nm) and also greatly suppress the formation of $MoS(e)_2$ layer (from ~350 to ~100 nm) and other harmful secondary phases. As a result, R_s was reduced from 1.83 to 1.54 $\Omega \cdot cm^2$, and FF was significantly enhanced from 42.67% to 52.12%. Additionally, a MoO_3 nanolayer improved the CZTSSe absorber quality by lowering the defect energy levels from 228 to 148 meV, which was determined by admittance spectroscopy (AS). To fundamentally investigate the role of MoO_3 nanolayers at the back contact of CZTSSe solar cells, a first-principles study was conducted using the Vienna Ab initio Simulation Package (VASP) [29–31]. Calculations reveal that the partial sulfoselenized MoO_3 nanolayers may be treated as a hole-selective contact between Mo/CZTSSe interfaces, and is beneficial for the device performance. Lastly, we demonstrate that introducing an ultrathin MoO_3 sacrificial nanolayer remarkably improved the CZTSSe absorber's quality, and optimized the back contact interface between CZTSSe and Mo, leading to the enhancement of overall solar cell performance.

2. Experimental Details

Multimetallic stacked Sn/Zn/Cu (CZT) precursor film of 600 nm thick was deposited onto a 1 μm Mo-coated (with/without ultrathin MoO_x nanolayers) soda-lime glass (SLG) substrate using the RF magnetron sputtering process. To synthesize CZTSSe absorbers, the CZT precursor films were annealed in a semisealed graphite box (7 cm^3 in volume) with Se pellets at a temperature of 550 °C for 7 mins in 20% H_2S (99.95%) diluted with Ar (99.99%) at atmospheric pressure (Cu/Sn + Zn ~0.9 and Zn/Sn ~1.14 measured by X-ray fluorescence (XRF), XRF-1800, Shimadzu Scientific Instrument). The *p*–n heterojunction was formed by depositing 40 nm CdS buffer layer on top of CZTSSe film using chemical bath deposition method. A 300 nm DC-sputtered ITO/40 nm ZnO contact was then directly deposited onto CdS/CZTSSe films. Lastly, a 300 nm Ag top metal contact and 100 nm MgF_2 antireflection coating were deposited on top of all devices by thermal evaporation. The device area (~0.105 cm^2) was defined by shadow masks and mechanical scribing, resulting in a cell

effective area of ~0.095 cm^2 [10,11]. The current density–voltage (J–V) characteristics of the solar cell devices were measured using a Keithley 2400 source meter under the illumination of an AM 1.5G Solar Simulator (Newport) with light intensity of 100 mW/cm^2, which was calibrated with an NREL-traceable Si reference cell. The spectral response and the external quantum efficiency (EQE) of cells were obtained using an ENLI Technology model EQE-D-3011 system. Temperature-dependent (120–300 K) capacitance–frequency (C–F) measurements were conducted by an Agilent E4980A LCR meter in the frequency range of 10^2–10^6 Hz at 0 V with an AC amplitude of 30 mV under dark conditions [32].

3. Results and Discussion

To confirm the successful deposition of an ultrathin MoO$_x$ film on the Mo-coated SLGs, X-ray photoelectron spectroscopy (XPS) measurements were performed, as shown in Figure 1. For the pristine Mo-coated SLGs (red line), the peaks of Mo3d$_{5/2}$ and Mo3d$_{3/2}$ were located at 228.3 and 231.5 eV, respectively, with a 3.2 eV energy difference, consistent with the literature values [33], indicating that there was almost no native metal oxide on the pristine Mo-coated SLGs. Once some MoO$_x$ had been thermally evaporated on the Mo-SLG substrates, except for the residual small peaks located at 228.3 eV (Mo3d$_{5/2}$ for pristine Mo), these XPS peaks were shifted to 232.9 eV (Mo3d$_{5/2}$ for MoO$_3$) and 236.1 eV (Mo3d$_{3/2}$ for MoO$_3$), respectively, with 3.2 eV energy difference, demonstrating that 5 and 10 nm ultrathin MoO$_3$ (not MoO$_2$) nanolayers were successfully deposited on the Mo substrates. Moreover, the ultrathin MoO$_3$ layers can be prepared by the reactive sputtering of 1 μm thick Mo on SLGs, which is compatible with the subsequent fabrication for CIGSSe solar cells [34].
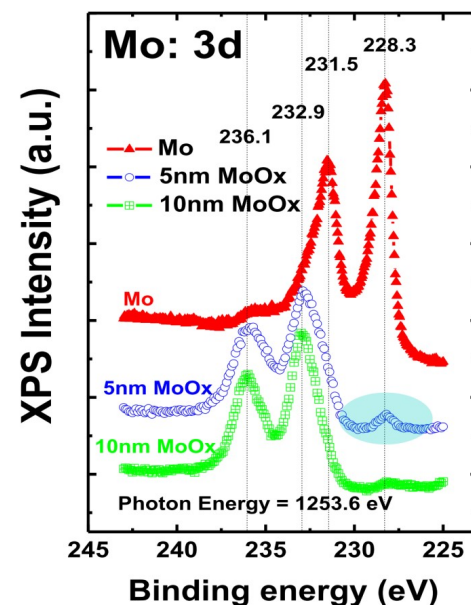
Figure 1. XPS spectra of thermally evaporated 0, 5, and 10 nm MoO$_x$ on Mo-SLG substrates.

The 600 nm thick Sn/Zn/Cu (CZT) multimetallic stacked precursors were sputtering-deposited on our Mo-SLGs with or without MoO$_3$ layers [11,35]. The X-ray diffraction (XRD) of metal stacked precursors on Mo-SLGs (in Figure 2) showed two characteristic peaks of well-intermixed metal alloys at 30.26°, corresponding to bronze (Cu$_6$Sn$_5$ JCPDS no. 45–1488), and 43.26°, belonging to brass (Cu$_5$Zn$_8$ JCPDS no. 25–1288). Along with these two phases, the characteristic peaks of Sn were also found at 30.71°, 32.10°, 43.95°, and 44.97° (JCPDS No. 650296). The well-intermixed precursors are beneficial to the CZTSSe growth during sulfoselenization [11,35].
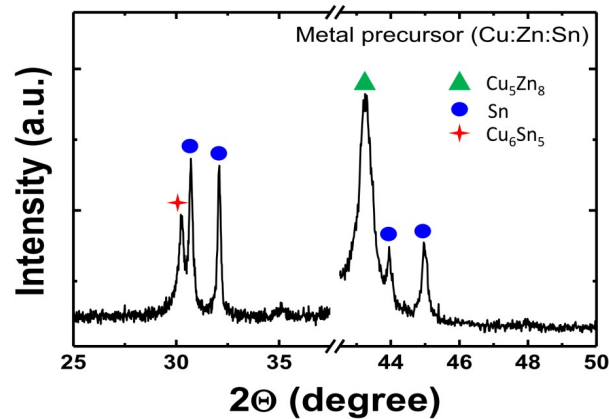
Figure 2. XRD of Sn/Zn/Cu (CZT) multimetallic stacked precursors on Mo-SLG substrates.

Raman spectroscopy with 473 nm wavelength excitation (around ~550 nm sampling depth) was conducted to examine the quality of CZTSSe films, as displayed in Figure 3. The signatures at 176, 207, and 239 cm^{-1} correspond to the CZTSe vibration modes, and the peak at 329 cm^{-1} corresponds to the CZTS vibration mode [11,35,36]. No peak shifts or secondary phases were observed between the pristine and 5 or 10 nm MoO$_3$-modified CZTSSe films. The progressive peak sharpening suggests the better quality of CZTSSe films grown on MoO$_3$ modified substrates compared with the pristine one. The Raman spectra can also be utilized to determine the sulfur and selenium (S/Se) ratio in the CZTSSe by taking the ratio of the peak shift for the sulfide based of the pure CZTS (338 cm^{-1}) and selenide based on the pure CZTSe (196 cm^{-1}) [9]. By calculating the ratio of the peak shift for sulfide-based (329 cm^{-1}) and selenide-based (207 cm^{-1}), an [S]/[S] + [Se] value of ~0.45 was obtained, leading to the S/Se ratio of 45:55.
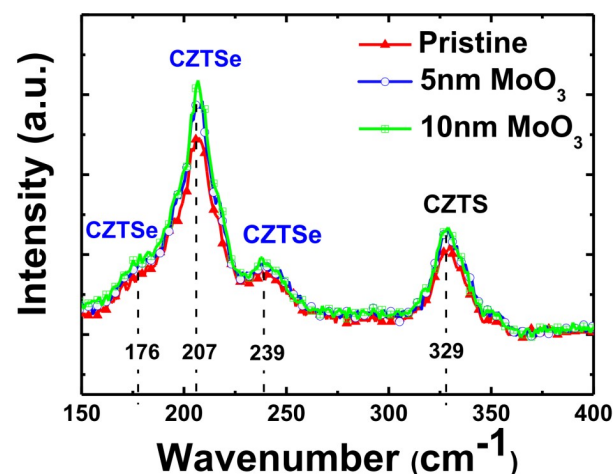
Figure 3. Raman spectra of CZTSSe grown on the Mo-SLGs without MoO$_3$, with 5 and 10 nm MoO$_3$ sacrificial nanolayers.

To investigate the MoO$_3$ effects on solar cell performances, the light J–V was measured on all the devices, as shown in Figure 4. For statistical study, there were 10 device cells for each condition. The average device performance and standard deviations (±) for different device conditions are summarized in Table 1. All cells with MoO$_3$ nanolayers exhibited higher short circuit current (J$_{SC}$), V$_{OC}$, and FF compared to the reference cells. The significant improvements in Voc from 450 to 473 mV, J$_{SC}$ from 25.86 to 27.33 mA/cm^2, and FF from 42.67% to 52.12% for devices inserted with a 5 nm MoO$_3$ layer were attributed to the increased shunt resistance (R$_{SH}$) from 145 to 151 Ω·cm^2 and the reduced R$_S$ from 1.83 to 1.54 Ω·cm^2, which may have resulted from the improvement in back contact quality.

Lastly, a CZTSSe solar cell with 7.78% PCE was obtained by inserting 5 nm MoO_3 layers, which was an improvement of about 26% compared with 5.76% PCE of the pristine one.
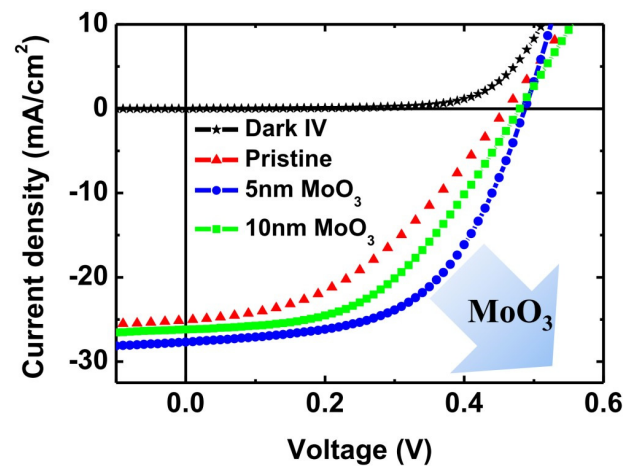
Figure 4. Current density–voltage (J–V) characteristics of CZTSSe devices without MoO_3, with 5 and 10 nm MoO_3 sacrificial nanolayers.

Table 1. Solar cell parameters of CZTSSe devices with different thickness of MoO_3.

	PCE (%)	J_{SC} (mA/cm^2)	V_{OC} (mV)	FF (%)	R_S ($\Omega \cdot$cm^2)	RSH ($\Omega \cdot$cm^2)
Pristine	5.21 ± 0.66	25.86 ± 2.26	450 ± 15	42.67 ± 1.5	1.83 ± 0.44	133 ± 45
5 nm MoO_3	6.80 ± 0.85	27.33 ± 2.20	473 ± 5	52.12 ± 3.0	1.54 ± 0.23	153 ± 68
10 nm MoO_3	6.49 ± 0.55	26.30 ± 1.57	474 ± 7	50.69 ± 1.5	1.77 ± 0.26	252 ± 63
Best cell (5 nm MoO_3)	7.78	28.84	480	55.83	1.68	180

Statistics from 10 cells for each condition.

To inspect the CZTSSe absorber quality near the Mo back contacts, cross-sectional TEM and EDS mapping was executed, as presented in Figures 5 and 6, respectively. $MoS(e)_2$ thickness was reduced from ~350 to ~100 nm, and CZTSSe grain sizes were enlarged by inserting 5 nm MoO_3 layers (Figure 5). In the pristine absorber, the void formation near the back contacts may have arisen from the vaporization of highly volatile secondary phases (i.e., Sn_xS and Sn_xSe_y) during the focused ion beam (FIB) fabrication of TEM samples. A large number of voids from secondary phases forming at the back interface limited the free-carrier transportation, leading to higher R_S and thereby lower J_{SC} [21]. EDS mapping (Figure 6) also directly illustrates the formation of unwanted secondary phases, such as Cu_xS_y, Zn_xS_y, Sn_xS_y, and Sn_xSe_y, near the untreated Mo back contacts, which further proves that the CZTSSe/Mo interface was chemically unstable [19]. However, the inserted MoO_3 nanolayers could not be identified by the oxygen/molybdenum elemental mapping images in Figure 6b. MoO_3 nanolayers may have been fully sulfoselenized to *p*-type $MoS(e)_{2-x}O_x$ during a high-temperature synthesis process. Therefore, the increased V_{OC} and FF, and reduced R_S in the modified devices may have been due to the larger grains of the CZTSSe absorber (i.e., fewer grain boundary recombination centers), the suppression of some harmful secondary phases, and the thinner $MoS(e)_2$ by inserting MoO_3 sacrificial nanolayers.
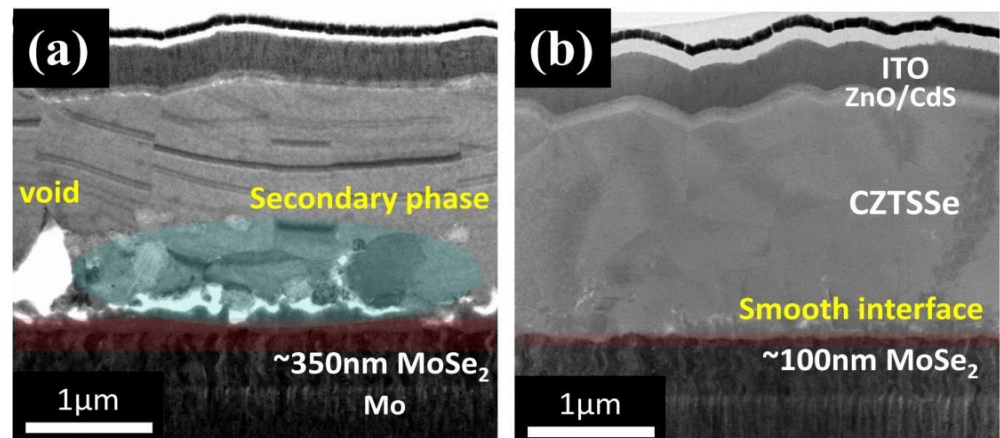
Figure 5. Cross-sectional TEM images of CZTSSe devices (**a**) without MoO_3 and (**b**) with 5 nm MoO_3 sacrificial nanolayers.
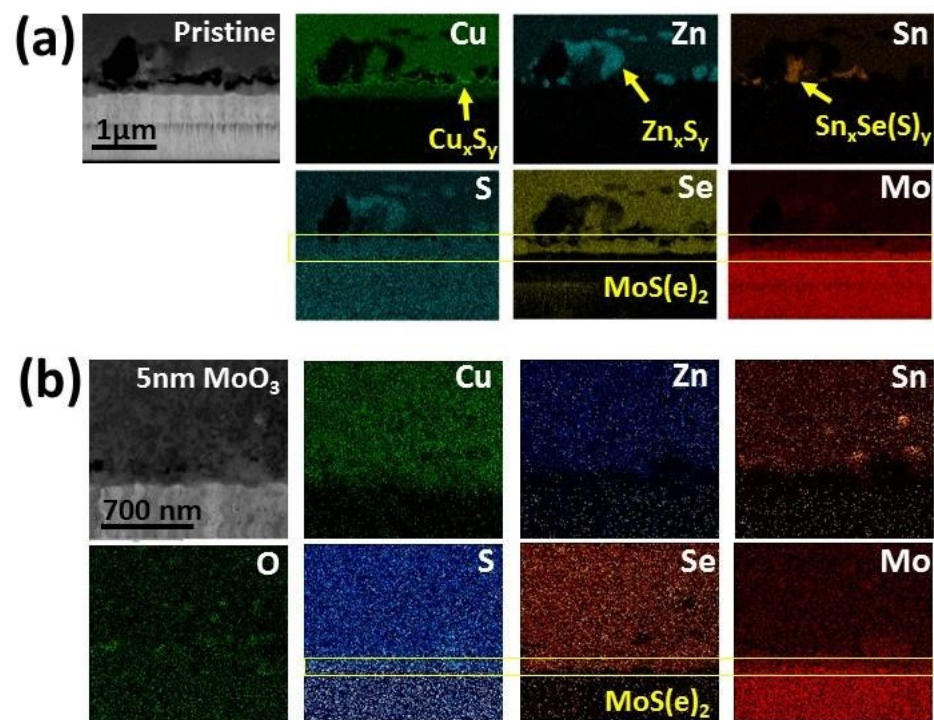
Figure 6. Elemental mapping images of CZTSSe films grown on the Mo-SLGs (**a**) without MoO_3 and (**b**) with 5 nm MoO_3 sacrificial nanolayers.

To understand why the device performance was not monotonically improved as MoO_3 thickness increased, cross-sectional TEM analysis was conducted, as shown in Figure 7. Inserting 10 nm MoO_3 increased the Rs, and reduced the J_{SC} and FF, thus decreasing the overall PCE (Table 1). The TEM results (Figure 7) show that the orientation of $MoS(e)_2$ can be vertically or horizontally aligned with the Mo substrate, which can provide different contact resistances. On the basis of the direction of the photocarrier separation (i.e., built-in electric field direction), the vertically aligned $MoS(e)_2$ was more conductive than the horizontally aligned one is. In fact, $MoS(e)_2$ is a layered material with a weak van der Waals bond between each layer; thus, its interlayer (i.e., horizontally aligned) conductivity is two orders of magnitude lower than its intralayer (i.e., vertically aligned) conductivity (Figure 7) [37–39]. The vertically aligned $MoS(e)_2$ came from the pristine Mo contact that reacted with S/Se vapor during the annealing process, while the horizontally aligned $MoS(e)_2$ came from the MoO_3 layers that lost their oxygen during the sulfoselenization

process due to the high vapor pressure of S/Se [40]. Therefore, it is preferable that the MoO_3 layers be transformed into horizontally aligned $MoS(e)_2$ (or $MoS(e)_{2-x}O_x$) because it can hinder S/Se diffusion during annealing process [40]. Hence, undesirable $MoS(e)_2$ thickness can be minimized. This shows that the higher Rs of 1.77 $\Omega \cdot cm^2$ for 10 nm MoO_3 devices compared with 1.54 $\Omega \cdot cm^2$ for 5 nm MoO_3 devices was due to a thicker MoO_3 that transformed into a more horizontally aligned $MoS(e)_2$. As a result, J_{SC} was reduced from 27.33 to 26.30 mA/cm^2 by inserting the thicker MoO_3, as shown in Table 1.
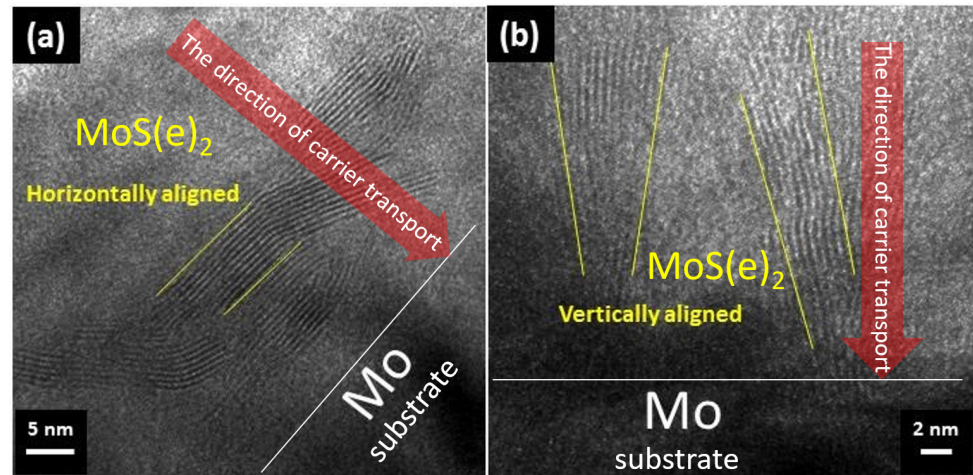
Figure 7. Cross-sectional TEM of (**a**) MoO_3-modified and (**b**) pristine Mo/CZTSSe interfaces for determining the $MoS(e)_2$ orientations relative to the Mo substrates.

To further study the effect of the MoO_3 sacrificial layer on defect states in CZTSSe, AS measurement was performed [32]. Figure 8 reveals the C–F profiling for CZTSSe devices with MoO_3 thickness of 0, 5, and 10 nm. Using the model in the work of Kimerling [41,42], capacitance at a high frequency represents the response of the free carrier density, while capacitance at a low frequency represents the response of the sum of free carriers and deep traps. The Arrhenius plot (Figure 9) was used to determine the activation energy of deep trap states with various MoO_3 thickness levels. For each AS spectrum, the inflection point frequency (or step frequency ω_0) is determined by applying angular frequency at the maximum of the $\omega dC/d\omega$ plot. The inflection point frequency of each AS spectrum can be used to construct the Arrhenius plot by fitting the spectra according to the following equation:

$$\omega_0 = 2\pi \nu_0 T^2 exp\left(\frac{E_a}{kT}\right)$$

where ω_0 is the step frequency, E_a is the energetic depth of the defect relative to the corresponding band edge, ν_0 is the pre-exponential factor comprising temperature-independent parts such as defect capture cross-sections for holes σ_p, thermal velocity ν_{th}, and the effective density of states in the valence band N_v.

Activation energy E_a ascertained with the Arrhenius plot was approximately the energy difference between the defect level and the valence band edge. Assuming that their energy levels were within a small range, the E_a value deduced from the Arrhenius plot could also represent the average value of activation energies of a band of defects in the band gap. The activation energies of CZTSSe devices with MoO_3 thicknesses of 0, 5, and 10 nm were 228, 148, and 199 meV, respectively (Figure 9). Both results support the argument that, besides suppressing $MoS(e)_2$ and secondary formation at the back interface, introducing MoO_3 as a sacrificial nanolayer may help in improving CZTSSe absorber quality by not only increasing the grain growth, but also lowering the activation energy of defect states.
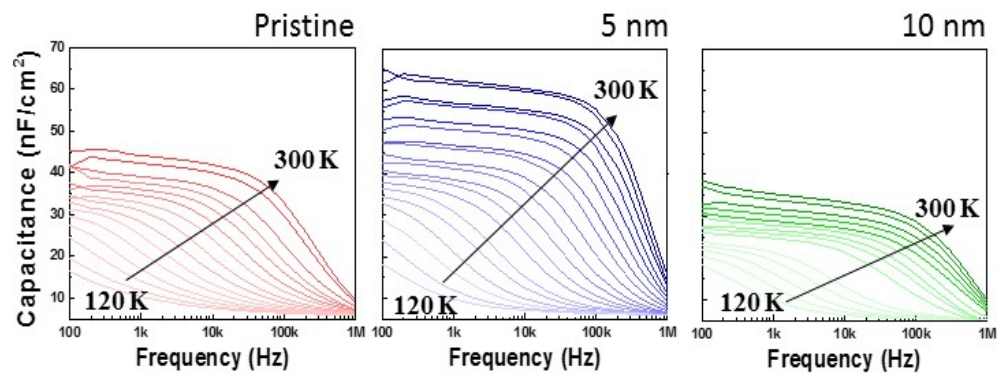
Figure 8. Admittance spectra of CZTSSe devices with different thickness levels of MoO$_3$.
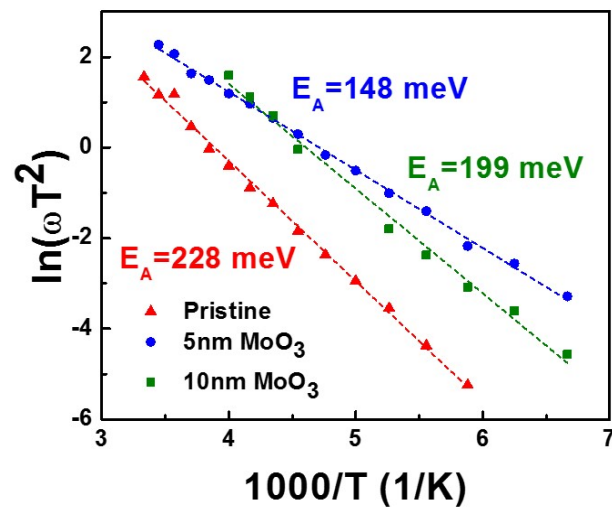
Figure 9. Arrhenius plot of the characteristic frequencies to extract the activation energy of CZTSSe devices with different thickness levels of MoO$_3$.

To fundamentally investigate the role of MoO$_3$ nanolayers at the back contacts of CZTSSe solar cells, first-principles calculations were conducted through VASP [29–31] to examine the electronic properties of S-doped MoO$_3$. The projector-augmented wave (PAW) method was adopted, and Perdew–Burke–Ernzerhof (PBE) exchange correlation functionals were used to account for electron–electron interactions in our system [43]. Monkhorst–Pack K-point grids of 2 × 2 × 2 and 400 eV energy cutoff for plane wave basis set were used for geometric optimization. The geometric structures were entirely relaxed when the total energy was converged to 10^{-6} eV in the 3 × 2 MoO$_3$ supercell model. The density-of-states (DOS) calculation of S-doped MoO$_3$ was performed using the same parameters except for the 6 × 6 × 6 Monkhorst–Pack K-point grids. Due to sulfidation, sulfur appeared in MoO$_2$, and this could be regarded as a sulfur substitution for oxygen in which three different sites substitutive defects could be formed, denoted as S$_{O1}$, S$_{O2}$, and S$_{O3}$. S$_{O1}$ is single oxygen coordinated, while S$_{O2}$ and S$_{O3}$ are double and triple oxygen coordinated, respectively, as shown in Figure 10.

Figure 11 reveals the DOS of MoO$_3$ with S$_O$ defects, which indicates that there were additional defective states (left-hand side near 0 eV) with slightly higher energy than that of the valence band maximum (VBM). There was no significant difference between sulfurization and selenization for MoO$_3$. The small difference was that the additional defective states of selenization were a little serious compared with the sulfurization one. The calculated DOS was almost the same for these three different defect sites, which means that the DOS was not sensitive to the chemical environment of S$_O$, and only one is shown. These defective S$_O$ states above the VBM, which contribute to the *p*-type carriers (holes) within the partial sulfoselenized

MoO_3 nanolayers, may be treated as hole-selective contacts between Mo/CZTSSe interfaces, further improving the overall PCE, as demonstrated experimentally.
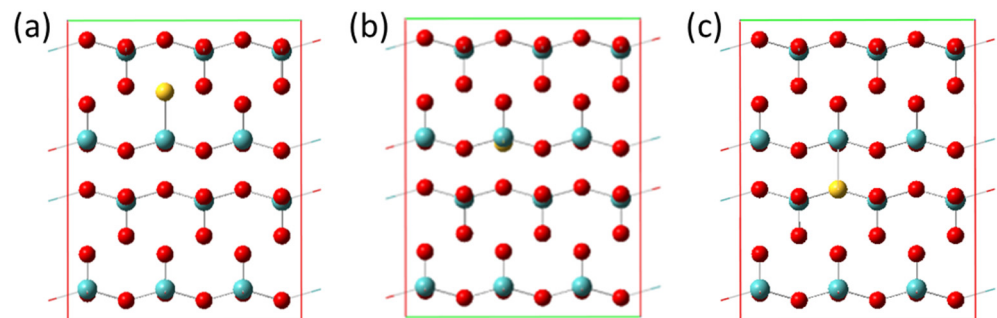
Figure 10. The optimized structure of MoO_3 containing (**a**) S_{O1}, (**b**) S_{O2}, and (**c**) S_{O3} defects.
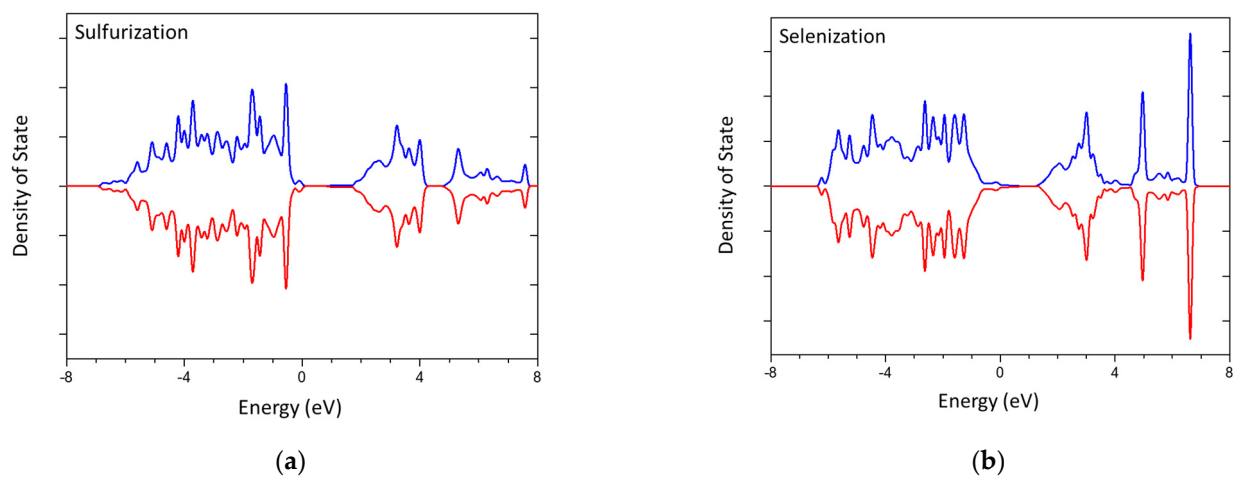
Figure 11. DOS of MoO_3 with S_O defects for (**a**) sulfurization and (**b**) selenization. The energy levels of defective states from S_O defects were slightly higher than those of VBM.

4. Conclusions

While CZTSSe is a very promising alternative for CdTe and CIGSSe for thin-film solar cells, its V_{OC} deficit and low FF critically obstruct the PCE. The formation of many harmful secondary phases at the back interface between CZTSSe and Mo leads to high series resistance (Rs), thus degrading overall solar cell performance. In this study, a MoO_3 nanolayer was applied as a sacrificial layer to optimize the back contact interface between CZTSSe and Mo. Cross-sectional TEM and EDS results show that the MoO_3 sacrificial nanolayers not only improved CZTSSe grain growth, but also successfully suppressed the formation of an undesirable $MoS(e)_2$ layer (from ~350 to ~100 nm) and other harmful secondary phases. From the device point of view, the Rs was reduced from 1.83 to 1.54 $\Omega \cdot cm^2$ and the FF was significantly increased from 42.67% to 52.12%, resulting in an increase in Voc by 23 mV. Importantly, MoO_3 nanolayers also improved CZTSSe absorber quality by lowering the defect energy levels from 228 to 148 meV. In addition to the experimental results, the first-principles calculations revealed that the partial sulfoselenized MoO_3 nanolayers may be treated as the (*p*-type) hole-selective contacts between Mo/CZTSSe interfaces, contributing to an overall improvement in device performance. Lastly, a CZTSSe solar cell with 7.78% PCE was obtained by inserting 5 nm MoO_3 nanolayers, which was an improvement of about 26% compared with the 5.76% PCE of the pristine one.

Author Contributions: C.-Y.C. and S.K. contributed equally for the first authorship. C.-Y.C., S.K. and W.-C.C. conceived the original idea and research plan. C.-Y.C. and S.K. conceived the presented idea, carried out the experiment, analyzed the results, and wrote the manuscript. Y.-R.L. and S.K. conducted the AS experiments. W.-C.C. executed the XRD. C.-Y.C. and W.-C.C. analyzed the TEM

characterization. J.-W.L. and P.-T.C. performed the simulation with first-principles calculations. C.-Y.C., K.-H.C. and L.-C.C. supervised this project. All authors discussed the results and contributed to the final manuscript. All authors have read and agreed to the published version of the manuscript.

Institutional Review Board Statement: Not applicable.

Informed Consent Statement: Not applicable.

Data Availability Statement: Not applicable.

Conflicts of Interest: The authors declare no conflict of interest.

References

1. Green, M.A.; Hishikawa, Y.; Dunlop, E.D.; Levi, D.H.; Hohl-Ebinger, J.; Yoshita, M.; Ho-Baillie, A.W.Y. Solar cell efficiency tables (Version 53). *Prog. Photovolt. Res. Appl.* **2019**, *27*, 3–12. [CrossRef]
2. Jackson, P.; Wuerz, R.; Hariskos, D.; Lotter, E.; Witte, W.; Powalla, M. Effects of heavy alkali elements in Cu(In,Ga)Se$_2$ solar cells with efficiencies up to 22.6%. *Phys. Status Solidi (RRL) Rapid Res. Lett.* **2016**, *10*, 583–586. [CrossRef]
3. Chirila, A.; Reinhard, P.; Pianezzi, F.; Bloesch, P.; Uhl, A.R.; Fella, C.; Kranz, L.; Keller, D.; Gretener, C.; Hagendorfer, H.; et al. Potassium-induced surface modification of Cu(In,Ga)Se$_2$ thin films for high-efficiency solar cells. *Nat. Mater.* **2013**, *12*, 1107–1111. [CrossRef] [PubMed]
4. Nakamura, M.; Yamaguchi, K.; Kimoto, Y.; Yasaki, Y.; Kato, T.; Sugimoto, H. Cd-Free Cu(In,Ga)(Se,S)$_2$ Thin-Film Solar Cell With Record Efficiency of 23.35%. *IEEE J. Photovolt.* **2019**, *9*, 1863–1867. [CrossRef]
5. Ginley, D.; Green, M.A.; Collins, R. Solar Energy Conversion Toward 1 Terawatt. *MRS Bull.* **2011**, *33*, 355–364. [CrossRef]
6. Butler, D. Thin Films: Ready for their close-up? *Nature* **2008**, *454*, 558–559. [CrossRef]
7. Katagiri, H.; Nishimura, M.; Onozawa, T.; Maruyama, S.; Fujita, M.; Sega, T.; Watanabe, T. Rare-metal free thin film solar cell. In Proceedings of the Power Conversion Conference, Nagaoka, Japan, 6 August 1997.
8. Katagiri, H.; Sasaguchi, N.; Hando, S.; Hoshino, S.; Ohashi, J.; Yokota, T. Preparation and evaluation of Cu$_2$ZnSnS$_4$ thin films by sulfurization of E-B evaporated precursors. *Sol. Energy Mater. Sol. Cells* **1997**, *49*, 407–414. [CrossRef]
9. Mitzi, D.B.; Gunawan, O.; Todorov, T.K.; Wang, K.; Guha, S. The path towards a high-performance solution-processed kesterite solar cell. *Sol. Energy Mater. Sol. Cells* **2011**, *95*, 1421–1436. [CrossRef]
10. Chen, C.-Y.; Aprillia, B.S.; Chen, W.-C.; Teng, Y.-C.; Chiu, C.-Y.; Chen, R.-S.; Hwang, J.-S.; Chen, K.-H.; Chen, L.-C. Above 10% efficiency earth-abundant Cu$_2$ZnSn(S,Se)$_4$ solar cells by introducing alkali metal fluoride nanolayers as electron-selective contacts. *Nano Energy* **2018**, *51*, 597–603. [CrossRef]
11. Chen, W.-C.; Chen, C.-Y.; Tunuguntla, V.; Lu, S.H.; Su, C.; Lee, C.-H.; Chen, K.-H.; Chen, L.-C. Enhanced solar cell performance of Cu$_2$ZnSn(S,Se)$_4$ thin films through structural control by using multi-metallic stacked nanolayers and fast ramping process for sulfo-selenization. *Nano Energy* **2016**, *30*, 762–770. [CrossRef]
12. Wang, W.; Winkler, M.T.; Gunawan, O.; Gokmen, T.; Todorov, T.K.; Zhu, Y.; Mitzi, D.B. Device Characteristics of CZTSSe Thin-Film Solar Cells with 12.6% Efficiency. *Adv. Energy Mater.* **2014**, *4*, 1301465. [CrossRef]
13. Scragg, J.J.; Watjen, J.T.; Edoff, M.; Ericson, T.; Kubart, T.; Platzer-Bjorkman, C. A detrimental reaction at the molybdenum back contact in Cu$_2$ZnSn(S,Se)$_4$ thin-film solar cells. *J. Am. Chem. Soc.* **2012**, *134*, 19330–19333. [CrossRef] [PubMed]
14. Shin, B.; Bojarczuk, N.A.; Guha, S. On the kinetics of MoSe$_2$ interfacial layer formation in chalcogen-based thin film solar cells with a molybdenum back contact. *Appl. Phys. Lett.* **2013**, *102*, 091907. [CrossRef]
15. Scragg, J.J.; Ericson, T.; Kubart, T.; Edoff, M.; Platzer-Björkman, C. Chemical Insights into the Instability of Cu$_2$ZnSnS$_4$ Films during Annealing. *Chem. Mater.* **2011**, *23*, 4625–4633. [CrossRef]
16. Nishiwaki, S.; Kohara, N.; Negami, T.; Wada, T. MoSe$_2$ layer formation at Cu(In,Ga)Se$_2$/Mo Interfaces in High Efficiency Cu(In1-xGax)Se$_2$ Solar Cells. *Jpn. J. Appl. Phys.* **1998**, *37*, 71–73. [CrossRef]
17. Shin, B.; Zhu, Y.; Bojarczuk, N.A.; Jay Chey, S.; Guha, S. Control of an interfacial MoSe$_2$ layer in Cu$_2$ZnSnSe$_4$ thin film solar cells: 8.9% power conversion efficiency with a TiN diffusion barrier. *Appl. Phys. Lett.* **2012**, *101*, 053903. [CrossRef]

18. Walsh, A.; Chen, S.; Wei, S.-H.; Gong, X.-G. Kesterite Thin-Film Solar Cells: Advances in Materials Modelling of Cu_2ZnSnS_4. *Adv. Energy Mater.* **2012**, *2*, 400–409. [CrossRef]

19. Scragg, J.J.; Kubart, T.; Wätjen, J.T.; Ericson, T.; Linnarsson, M.K.; Platzer-Björkman, C. Effects of Back Contact Instability on Cu_2ZnSnS_4 Devices and Processes. *Chem. Mater.* **2013**, *25*, 3162–3171. [CrossRef]

20. Liu, F.; Sun, K.; Li, W.; Yan, C.; Cui, H.; Jiang, L.; Hao, X.; Green, M.A. Enhancing the Cu_2ZnSnS_4 solar cell efficiency by back contact modification: Inserting a thin TiB_2 intermediate layer at Cu_2ZnSnS_4/Mo interface. *Appl. Phys. Lett.* **2014**, *104*, 051105. [CrossRef]

21. Zhou, F.; Zeng, F.; Liu, X.; Liu, F.; Song, N.; Yan, C.; Pu, A.; Park, J.; Sun, K.; Hao, X. Improvement of Jsc in a Cu_2ZnSnS_4 Solar Cell by Using a Thin Carbon Intermediate Layer at the Cu_2ZnSnS_4/Mo Interface. *ACS Appl. Mater. Interfaces* **2015**, *7*, 22868–22873. [CrossRef]

22. López-Marino, S.; Placidi, M.; Pérez-Tomás, A.; Llobet, J.; Izquierdo-Roca, V.; Fontané, X.; Fairbrother, A.; Espíndola-Rodríguez, M.; Sylla, D.; Pérez-Rodríguez, A.; et al. Inhibiting the absorber/Mo-back contact decomposition reaction in $Cu_2ZnSnSe_4$ solar cells: The role of a ZnO intermediate nanolayer. *J. Mater. Chem. A* **2013**, *1*, 8338–8343. [CrossRef]

23. Yin, Z.; Zhang, X.; Cai, Y.; Chen, J.; Wong, J.I.; Tay, Y.Y.; Chai, J.; Wu, J.; Zeng, Z.; Zheng, B.; et al. Preparation of MoS_2-MoO_3 hybrid nanomaterials for light-emitting diodes. *Angew. Chem.* **2014**, *53*, 12560–12565. [CrossRef]

24. Qin, P.; Fang, G.; Ke, W.; Cheng, F.; Zheng, Q.; Wan, J.; Lei, H.; Zhao, X. In situ growth of double-layer MoO_3/MoS_2 film from MoS_2 for hole-transport layers in organic solar cell. *J. Mater. Chem. A* **2014**, *2*, 2742–2756. [CrossRef]

25. McDonnell, S.; Azcatl, A.; Addou, R.; Gong, C.; Battaglia, C.; Chuang, S.; Cho, K.; Javey, A.; Wallace, R.M. Hole Contacts on Transition Metal Dichalcogenides: Interface Chemistry and Band Alignments. *ACS Nano* **2014**, *8*, 6265–6272. [CrossRef] [PubMed]

26. Yun, J.M.; Noh, Y.J.; Lee, C.H.; Na, S.I.; Lee, S.; Jo, S.M.; Joh, H.I.; Kim, D.Y. Exfoliated and partially oxidized MoS_2 nanosheets by one-pot reaction for efficient and stable organic solar cells. *Small* **2014**, *10*, 2319–2324. [CrossRef] [PubMed]

27. Chuang, S.; Battaglia, C.; Azcatl, A.; McDonnell, S.; Kang, J.S.; Yin, X.; Tosun, M.; Kapadia, R.; Fang, H.; Wallace, R.M.; et al. MoS_2 P-type transistors and diodes enabled by high work function MoO_x contacts. *Nano Lett.* **2014**, *14*, 1337–1342. [CrossRef] [PubMed]

28. Gao, S.; Jiang, Z.; Wu, L.; Ao, J.; Zeng, Y.; Sun, Y.; Zhang, Y. Interfaces of high-efficiency kesterite $Cu_2ZnSnS(e)_4$ thin film solar cells. *Chin. Phys. B* **2018**, *27*, 018803. [CrossRef]

29. Kresse, G.; Furthmüller, J. Efficiency of ab-initio total energy calculations for metals and semiconductors using a plane-wave basis set. *Comput. Mater. Sci.* **1996**, *6*, 15–50. [CrossRef]

30. Kresse, G.; Hafner, J. Ab initio molecular-dynamics simulation of the liquid-metal-amorphous-semiconductor transition in germanium. *Phys. Rev. B* **1994**, *49*, 14251–14269. [CrossRef]

31. Kresse, G.; Furthmüller, J. Efficient iterative schemes for ab initio total-energy calculations using a plane-wave basis set. *Phys. Rev. B* **1996**, *54*, 11169. [CrossRef]

32. Lin, Y.-R.; Tunuguntla, V.; Wei, S.-Y.; Chen, W.-C.; Wong, D.; Lai, C.-H.; Liu, L.-K.; Chen, L.-C.; Chen, K.-H. Bifacial sodium-incorporated treatments: Tailoring deep traps and enhancing carrier transport properties in Cu_2ZnSnS_4 solar cells. *Nano Energy* **2015**, *16*, 438–445. [CrossRef]

33. Moulder, J.F.; Stickle, W.F.; Sobol, P.E.; Bomben, K.D. *Handbook of X-ray Photoelectron Spectroscopy: A Reference Book of Standard Spectra for Identification and Interpretation of XPS Data*; Physical Electronics: Chanhassen, MN, USA, 1995.

34. Zhou, D.; Zhu, H.; Liang, X.; Zhang, C.; Li, Z.; Xu, Y.; Chen, J.; Zhang, L.; Mai, Y. Sputtered molybdenum thin films and the application in CIGS solar cells. *Appl. Surf. Sci.* **2016**, *362*, 202–209. [CrossRef]

35. Chen, W.-C.; Tunuguntla, V.; Li, H.-W.; Chen, C.-Y.; Li, S.-S.; Hwang, J.-S.; Lee, C.-H.; Chen, L.-C.; Chen, K.-H. Fabrication of $Cu_2ZnSnSe_4$ solar cells through multi-step selenization of layered metallic precursor film. *Thin Solid Film.* **2016**, *618*, 42–49. [CrossRef]

36. Gürel, T.; Sevik, C.; Çağın, T. Characterization of vibrational and mechanical properties of quaternary compounds Cu_2ZnSnS_4 and $Cu_2ZnSnSe_4$ in kesterite and stannite structures. *Phys. Rev. B* **2011**, *84*, 205201. [CrossRef]

37. Evans, B.L.; Young, P.A. Optical absorption and dispersion in molybdenum disulphide. *Proc. R. Soc. Lond. A* **1965**, *284*, 402–422. [CrossRef]

38. Hu, S.Y.; Liang, C.H.; Tiong, K.K.; Lee, Y.C.; Huang, Y.S. Preparation and characterization of large niobium-doped $MoSe_2$ single crystals. *J. Cryst. Growth* **2005**, *285*, 408–414. [CrossRef]

39. Laursen, A.B.; Kegnæs, S.; Dahl, S.; Chorkendorff, I. Molybdenum sulfides—Efficient and viable materials for electro-and photoelectrocatalytic hydrogen evolution. *Energy Environ. Sci.* **2012**, *5*, 5577. [CrossRef]

40. Kong, D.; Wang, H.; Cha, J.J.; Pasta, M.; Koski, K.J.; Yao, J.; Cui, Y. Synthesis of MoS_2 and $MoSe_2$ films with vertically aligned layers. *Nano Lett.* **2013**, *13*, 1341–1347. [CrossRef]

41. Kimerling, L.C. Influence of deep traps on the measurement of free-carrier distributions in semiconductors by junction capacitance techniques. *J. Appl. Phys.* **1974**, *45*, 1839–1845. [CrossRef]

42. Duan, H.-S.; Yang, W.; Bob, B.; Hsu, C.-J.; Lei, B.; Yang, Y. The Role of Sulfur in Solution-Processed $Cu_2ZnSn(S,Se)_4$ and its Effect on Defect Properties. *Adv. Funct. Mater.* **2013**, *23*, 1466–1471. [CrossRef]

43. Perdew, J.P.; Burke, K.; Ernzerhof, M. Generalized Gradient Approximation Made Simple. *Phys. Rev. Lett.* **1996**, *77*, 3865. [CrossRef] [PubMed]